The preeminent role of directional selection in generating extreme morphological change in Glyptodonts (Cingulata; Xenarthra)

Fabio A. Machado[a,1], **Gabriel Marroig**[b], **and Alex Hubbe**[c,1]

[a]Department of Biology, Virginia Tech, USA.; [b]Departamento de Genética e Biologia Evolutiva, Instituto de Biociências, Universidade de São Paulo, Brazil.; [c]Departamento de Oceanografia, Instituto de Geociências, Universidade Federal da Bahia, Brazil

This manuscript was compiled on July 7, 2021

The prevalence of stasis on paleontological and comparative data has been classically taken as evidence of the strong role of stabilizing selection in shaping morphological evolution. When confronted against biologically informed predictions, empirical rates of evolution tend to fall below what is expected under genetic drift, suggesting that the signal for directional selection is erased at longer time scales. However, empirical tests of these claims are few and tend to focus on univariate traits, ignoring the potential roles of trait covariances in constraining evolution. Here we investigated the multivariate rates of morphological evolution in a fossil lineage that underwent extreme morphological modification, the glyptodonts. Contrary to what was expected, biologically informed models of evolution suggest a preeminent role of directional selection on the divergence of glyptodonts from living armadillos. Furthermore, the reconstruction of selection patterns shows that traits selected to generate a glytodont morphology are markedly different from those necessary to explain the extant armadillos' morphological diversity. Changes in both direction and magnitude of selection are probably tied to the invasion of a specialist-herbivore adaptive zone by glyptodonts. These results suggest that directional selection might have played a more important role in the evolution of extreme morphologies than previously imagined.

Skull | Extreme morphology | Fossil | Natural selection | Rates of Evolution |

DRAFT

Identifying signals of adaptive evolution using rates of change on a macroevolutionary scale is inherently problematic because tempo and mode of evolution are intertwined. While stabilizing selection slows down phenotypic change, directional selection can produce faster rates of evolution (1–3). This means that the action of selection (directional or stabilizing) can be identified by contrasting how fast species evolve to the expected rates under genetic drift (1, 2). While this framework has been successfully applied to microevolutionary time scales (4), its usefulness to macroevolutionary and deep-time studies has been contentious (5).

At larger time scales, it is challenging to quantify the effect of directional selection on the evolutionary process. The leading mechanism of phenotypic evolution on the macroevolutionary scale is thought to be stabilizing selection, as attested by the prevalence of stasis in the fossil record (6). This does not necessarily mean that directional selection did not play any role in phenotypic diversification. In fact, because the adaptive landscape (the relation between phenotype and fitness) is thought to be rugged, with many different optimal phenotipic combinations (peaks), evolutionary change under directional selection is bound to be fast during peak shifts, and punctuated at the macroevolutionary scale (6). Thus, because stasis is so prevalent and measured rates of change reflect the net-evolutionary processes that operated during the course of lineages' histories, rates of evolution calculated on phylogenies and fossil record tend to be small when compared to rates observed in extant populations (5). As a result, measured net-evolutionary rates of morphological change are more commonly than not consistent with evolution under stabilizing selection or drift (3, 5, 7–10). This probably explains why macroevolutionary studies usually infer the action of directional selection indirectly through pattern-based methods (e.g., through peak-transitions in diffusion-like models (11); the comparison of rates of change between lineages (12), etc), rather than adopting biologically informed models (e.g. those derived from quantitative genetics theory).

While this departure from biologically informed model might be justified for univariate traits (5, 7, 10), there is a wealth of evidence showing that the evolution of multivariate complex phenotypes, such as the mammalian skull, follow rules of growth and inheritance that can be modeled using quantitative genetics theory (9, 14, 15). Complex morphological traits are composed of subunits that are interconnected to each other to varying degrees. These different degrees of interconnection, generated by

AH, FAM and GM formulated the original scientific questions. AH sampled all the data. FAM lead data analysis and wrote initial draft of the manuscript. GM provided resources for the completion of the project. All authors have contributed to the manuscript preparation.

The authors declare no conflict of interest.

[1] To whom correspondence should be addressed. E-mail: FAM: macfabio@gmail.com; AH: alexhubbe@yahoo.com

the complex interaction of multiple ontogenetic pathways, leads to an unequal distribution of variance among parts (16), which in turn results in constraints to adaptive evolution (1, 3, 17, 18). Ignoring the possible role of constraints on the evolution of morphology can have many potential drawbacks, including the establishment of unrealistic expectations for drift in certain directions of the morphospace (3, 19), and possibly obscuring the signal of directional selection. To investigate the effect of directional selection on macroevolutionary scales, while avoiding potential pitfalls inherit to the analysis of multivariate traits, one should aim at studying a complex trait with well known trait covariance structure and that probably experienced high rates of evolutionary change. One such example is the case of the evolution of the glyptodont skull.

Glyptodonts originated in South America and are members of the order Cingulata (Xenarthra, Mammalia), which also includes the extant armadillos. An emblematic characteristics of glyptodonts that is shared with all members of this order is the presence of an osteoderm-based exoskeleton (20). However, glyptodonts have a set of unique traits that makes them stand out from all other mammals, including defensive tail weaponry, large size and, specifically, a highly modified skull. Glyptodonts skull has undergone a particular process of telescoping in which the rostrum is ventrally expanded, and the tooth row is posteriorly extended, resulting in a structure with biomechanical proprieties that are unprecedented among mammals (21, 22). These changes are thought to have arisen by the drastic change in ecology of glyptodonts in relation to other Cingulata. While most extant and fossil armadillos fall within a generalist-insectivore spectrum of diet, glyptodonts are believed to have been fully herbivorous, thus inhabiting a different adaptive zone (i.e. a region of the morphospace defined by similar ecological roles, (23, 24)) than armadillos (21, 22). Because of this unique morphology, glyptodonts' phylogenetic position has been historically uncertain (20, 25, 26). Classically, they have been regarded as a sister group to extant armadillos. However, recent ancient DNA analysis studies support that glyptodonts are nested within the extant armadillo clade, having originated during the late Miocene (13, 27). As such, glyptodonts evolved during the same period of time it took for different extant armadillo lineages to diversify, making this a perfect model to study morphological evolution in a restricted taxonomic scope. Furthermore, the covariance structure of cranial traits has been extensivelly investigated in mammals in general and in Xenarthra specifically (28), allowing one to investigate the evolution of cranial morphology in Glyptodonts while taking into account the potential constraining effects of among-traits integration.

The present contribution aims to use the unique glyptodont case to evaluate if we can identify the signal of directional selection on multivariate macroevolutionary data using biologically informed models of morphological evolution. Specifically, we calculate the empirical rates of evolution among Cingulata taxa and compare that to the expected rates of evolution under genetic drift to identify cases of extreme morphological evolution that can be confidently associated with directional selection. Additonally, we retrospectively estimate the selective forces necessary to generate all morphological diversification within Cingulata to better understand if evolutionary processes responsible for the evolution of glyptodonts are qualitatively different (i.e. selection guided glyptodonts in different directions) from those associated with other Cingulata taxa.

Results and Discussion

A principal component analysis (PCA) of our full multivariate dataset of skull measurements (860 specimens from 15 species including two *Glyptodon* specimens; Table S1) illustrates the uniqueness of glyptodontinae morphology (Figure 1A). Glyptodontinae shows an extreme score on PC1 in comparison to the extant armadillos,(Figure 1A-B), which is considered a size and allometric direction of the morphospace (Table S2)(29). The giant armadillo *Priodontes maximus* also presents a high score on PC1, but with values that are still closer to the remaining Cingulata than to *Glyptodon*. Dasypodidae species tend to occupy a different position of the morphospace than Euphractinae and Tolypeutinae, with similar PC1 values but smaller PC2 scores associated with an increase in the size of facial traits (Table S2). Despite these differences, extant armadillos are concentrated on a similar region of the morphospace (Figure 1A), which could be evidence that their morphology is being maintained within a "generalist-armadillo" adaptive zone, while glyptodonts invaded a new herbivore zone (24).

To evaluate the evolutionary processes involved in generating these morphological patterns, we employed Lande's generalized genetic distance (LGGD), which allows confronting observed rates of evolution to the expected rate under genetic drift, while taking into account the genetic association (covariances) among traits (1). The LGGD was calculated for the full morphological dataset (henceforth "form") as well as for allometry-free shape features (henceforth "shape") and size alone (henceforth "size"). LGGD values were obtained for the difference between the two daughter lineages for each node of the phylogeny (i.e., phylogenetic independent contrasts, or PIC) to control for phylogenetic dependence on the dataset (30).

Our results show that stabilizing selection was the dominant force in the morphological evolution of Cingulata (Fig. 2), a fact that is more evident for form and shape. For size, most observed LGGD values fell within the expected under drift. These results agree with previous evidence that stabilizing selection is the dominant evolutionary process shaping mammalian morphological diversification (5, 7, 9). Our results further indicate that stabilizing selection is more expressive for shape than for size, consistent with the idea that shape is more constrained by functional demands than size (31–33).

Nevertheless, while most nodes failed to exhibit values above the expected under drift, a noticeable exception was the one representing the divergence between Glyptodontinae and Tolypeutinae. This node presented LGGD values for form, shape, and size that fall above the expected under drift, suggesting that directional selection had a preeminent role during the divergence of this group. The multivariate PIC for this node and PC1 of the full dataset (Figure 1) are highly aligned (vector correlation=> 0.98), indicating that this PIC is mostly associated with the divergence of Glyptodonts from all remaining Cingulata. This increased evolutionary rate do not seem to be an artifact introduced the timing of the origin of Glyptodonts, as older nodes that are also associated with the divergence of subfamilies within Cingulata did not show elevated LGGD values (Fig. 2). In other words, while most of the evolution of Cingulata was kept within certain delimited morphological boundaries by

DRAFT

stabilizing selection, the radical morphological change and innovation found in glyptodonts was due to a remarkable increased importance of directional selection.

To inspect if the selective pressures necessary to generate a Glyptodont morphology differ from the remaining Cingulata in scale and direction (*i.e.*, which combination of traits are favored by natural selection), we calculated the selection gradients necessary to generate all divergence observed in our sample (10, 18). We then summarized this information by calculating the predominant directions of directional selection (18, 34, 35). This method is analogous to a PCA on selection gradients and allows the investigation of the combination of traits that were most favored by selection throughout the group's evolution. The first three leading eigenvectors of the covariance matrix of selection gradients (W_1, W_2 and W_3) were deemed significant (Fig. S5), but we focus on the first two vectors (Fig. 3) because W_3 is mostly associated with the within Euphractinae differentiation (Fig. S6)

The leading vector W_1 summarizes a selection for a reduction of the skull's total length while also showing a dorsoventral expansion of the face region, along with an increase in the tooth-row size. This description matches the telescoping process that Glyptodonts went through during their evolutionary history (21). Not surprisingly, the node associated with Glyptodonts' origin (node 21) not only scored heavily on this axis but is also strongly aligned with it (vector correlation=0.98), reinforcing that W_1 is a Glyptodont-exclusive combination of selective pressures. These results highlight that the selection necessary to generate the Glyptodont morphology is different from other Cingulata in both magnitude and direction. Changes in the orientation and strength of selection have been associated with dietary shifts in other mammals (35, 36), suggesting that the selective change observed in Glyptodonts has an ecomorphological basis.

The second vector, W_2, summarizes a contrasting selection on the face and the neurocranium. While these changes resemble patterns of allometric shape change common to all mammals (37), there is little size divergence between the nodes with high absolute scores on this axis. One possible exception is the divergence of *Priodontes* from the remaining Tolypeutinae (node 22, Fig. 2C). Thus, the selection summarized by W_2 might be associated with the face relative size, which could translate into subtle biomechanical differences, ultimately leading to ecomorphological adaptation to different dietary niches within the generalist-insectivore Cingulata adaptive zone (38). A similar pattern was described for Canidae, where the contrast between neurocranium and face was also recovered as a size-independent axis and tentatively associated with diet changes (35). The presence of a similar size-independent direction of selection in two distantly related mammalian groups suggests that the contrasting changes in the neurocranium and face might be a common selective phenomenon emerging from ecomorphological pressures.

Previous investigations on the macroevolutionary rates of morphological evolution in mammals have shown that morphological change is usually orders of magnitude slower than would be expected by drift (5). Such macroevolutionary rates are usually measured as the ratio between total morphological differentiation and time (30). As divergence times increase, even extreme changes can get diluted, implying that searching for signals of directional selection in macroevolutionary data might be futile. In this sense, our findings are striking, since we where able to identify the signal of directional selection on a divergence event that occurred 35mya ago. To our knowledge, a comparable signal was only previously found at the divergence between lower and higher apes, at 20mya, and the origin of humans, at 6mya (9). This is somewhat expected, as primates are marked by a phylogenetic trend towards increased brain size, a pattern that is intensified on hominins (39). The evolution of Glyptodontinae might also have been marked by a gradual and continuous differentiation: early representatives of the group, such as *Propalaehoplophorus*, exhibits an intermediary version of the cranial telescoping that is characteristic of latter glyptodonts (21). Thus, the evolution of glyptodonts can be the oldest and longest case of continuous and gradual differentiation in the fossil record. Alternatively, if the evolution of the group was punctuated by long periods of stasis, this could mean that directional selection events were even more intense than shown by the present analysis. Given the clear difference between primitive and derived forms within the group, the truth probably lies somewhere in between, with a gradual directional evolution punctuated by some periods of stasis.

As mentioned above, the use of biologically informed models for the investigations of evolutionary rates at macroevolutionary scales is still rare and limited in scope. We suggest that some of this dismissal comes from the assumed inapplicability of these models at larger time scales due to the overwriting power of stabilizing selection. Here we show that this assumption does not hold for glyptodonts, raising the possibility that directional selection is more pervasive than previously thought. The integration of more refined paleontological, demographic and life-history data in the investigation of macroevolutionary questions will lead to a more nuanced view of the role of directional and stabilizing selection on the evolution of complex morphologies.

Materials and Methods

Morphometrics and trait covariance. Morphometric analysis was based on 33 linear distances obtained from 3D cranial landmarks (figure S1) digitized from 860 museum collection specimens (Table S1). These measurements are designed to capture general dimensions of bones and structures of the mammalian skull. Landmarks and distances are based on (28). Traits were log-transformed to normalize differences in variance due to scale differences. Sample sizes ranged from 2-341 per species. We adopted the phenotypic covariance matrix (or $\mathbf{P}$) as a surrogate of the additive genetic covariance matrix $\mathbf{G}$ (see (28) for details). Here, we calculated $\mathbf{P}$ as the pooled within-group covariance matrix for all species. This assumes that the $\mathbf{P}$ is stable throughout the group's evolution (28). Expressly, we assume that the $\mathbf{P}$ for glyptodonts is the same as for the rest of Cingulata. While this might be contentious due to the extreme morphological modification in the group, $\mathbf{P}$s were shown to be similar among extant and fossil Xenarthra, including giant ground sloths (28). Additionally, because glyptodonts are nested within extant Cingulata, using the pooled covariance for living species as a model for glyptodont can be seen as a case of phylogenetic bracketing (40).

DRAFT

Form (shape+size) was quantified as the full morphospace, while shape was obtained by projecting out the leading PC of the within-group $\mathbf{P}$ the dataset. Given that PC1 is usually a size direction (i.e. where all loadings show similar values and the same sign 29; Tab. S2), this produces a dataset that is free from both size and allometric variation. Size was quantified as the geometric mean of all traits for each individual. Morphological variation for form was described with a principal component analysis (PCA) for cranial data (Fig 1, Tab S2).

Mode of evolution. To evaluate the mode of evolution along specific parts of the phylogenetic tree, we employed Lande's generalized genetic distance (LGGD) (1):

$$LGGD = \frac{N_e}{t}\Delta z^t \mathbf{G}^{-1}\Delta z \qquad [1]$$

where Δz is the phenotypic evolution that happened during a period of time, t is the time in generations, N_e is the effective population size and $\mathbf{G}$ is the additive genetic covariance matrix among traits. Here we used time-standardized Phylogenetic Independent Contrasts (PIC) as an estimate of Δz (41), which means that Δz is given as the rate of evolution that operated during the divergence of the two daughter lineages emerging from a node.

For this analysis, the phylogeny was scaled so the divergence time is given in generations instead of Myr. Generation times were set to be equal to the timing of sexual maturity of females plus the incubation period as a conservative estimate. We do not assume any reproductive seasonality. To obtain generation times for species without data on life-history traits (fossil species included), we estimated the linear relationship (in log scale) of body mass and generation time for 805 mammal species (42). Body mass values were then used to estimate generation times. Because Cingulata shows a proportionally shorter generation time than the linear trend for all mammals, we subtracted a constant to correct for that difference (Fig S2). Given that *Glyptodon* body mass estimates can vary, ranging from 819kg to 2000kg (22, 43), we calculated generation times for these extreme values. This resulted in generation times estimates ranging from 3.8-4.6 years, consistent with generation times for large ungulates (42, 44). We reconstructed ancestral values for generation time using maximum likelihood (45). Each branch length was then divided by the average between the ancestral and descendent generation times to scale the phylogeny.PIC values obtained in the scaled phylogeny are given in units $\Delta z/t$.

Since there is little available information for the N_e of Cingulata, we sampled N_e values from a uniform distribution ranging from 10,000 to 300,000. Estimates of effective population sizes for other Late Quaternary large herbivores range from 15,000-790,000 (44), so the values chosen here can be seen as conservative estimates in the case of glyptodonts. To approximate $\mathbf{G}$, we employed the Cheverud Conjecture (46), which states that the pattern of phenotypic covariances $\mathbf{P}$ can be used as a proxy for $\mathbf{G}$ when certain conditions are met (28). Because $\mathbf{P}$s contain more variance than $\mathbf{G}$s, we scaled the latter according to a constant which, in the case of perfect proportionality between matrices, is equal to the average heritability ($\bar{h^2}$) of all traits (9). Values for $\bar{h^2}$ were drawn from a uniform distribution ranging from 0.3 and 0.6, which are compatible with heritability estimates for the same cranial traits in other mammalian species (47, 48). Thus, we produced a range of LGGD values for each node to account for uncertainty on both N_e and $\bar{h^2}$.

Because parametric methods had an inadequate type I error rate (see Fig S3), a null distribution of LGGD was constructed by simulating multivariate evolution under genetic drift as follows

$$\mathbf{B} = \frac{t}{N_e}\mathbf{G} \qquad [2]$$

where $\mathbf{B}$ is the covariance matrix between evolutionary changes (1). For each simulation, the randomly generated value of N_e was used to construct a $\mathbf{B}$ from which one observation would be drawn for one generation ($t = 1$). This procedure was repeated 10000 times to generate a null distribution under drift. Values below 2.5% of the simulated values are considered to be dominated by stabilizing selection and values above 97.5% of the simulated values are considered to be dominated by directional selection.

Note that estimated rates in a macroevolutionary context are better seen as the net effect of the sum of all evolutionary processes that acted during the history of a lineage (49). Thus, instead of classifying lineages under either directional or stabilizing selection (or drift), our results should be seen as an investigation of the relative importance of these multiple processes.

Reconstruction of past selection. We investigate multivariate patterns of selection by calculating the selection gradient β relative to each node of the phylogeny. β is a vector of partial slope coefficients of fitness on the phenotype and can be estimated using a version of the multivariate Breeder's equation

$$\beta = \mathbf{G}^{-1}\Delta z \qquad [3]$$

with Δz being the PICs obtained at each node. We applied an extension on eigenvalues after the 21st to minimize the effect of noise in the calculation of β (50) (see supplementary material; Figure S4). To summarize multiple βs, we performed an analysis similar to PCA, in which node-wise βs are projected on the two leading lines of most selection (W_1 and W_2). This was done by calculating the matrix of average cross-product of βs (the matrix of covariance of realized adaptive peaks), extracting the leading eigenvectors from that matrix, and projecting individual βs on the subspace defined by these axes. The number of leading vectors was evaluated employing a simulation approach (35) (see supplementary material).

ACKNOWLEDGMENTS. We thank the curators of the following institutions for providing access to specimens and support for data acquisition: American Museum of Natural History; California Academy of Science; Faculdad de Ciencias de la Universidad de la Republica; Field Museum of Natural History; Museu Paraense Emílio Goeldi; Idaho Museum of Natural History; Los Angeles County Museum; La Brea Tar Pits and Museum; Museo Argentino de Ciencias Naturales; Museu de Ciências Naturais da Pontifícia Universidade Católica de Minas Gerais; Museu de Ciências Naturais da Fundação Zoobotânica do Rio Grande do Sul; Museo de La Plata; Museo Paleontológico de Colonia del Sacramento; Museu Nacional de Historia Natural de Montevideo; Museu Nacional (Rio de Janeiro); University of California Museum of Vertebrate Zoology; Natural History Museum (London); University of California Museum of Paleontology; Florida Museum of Natural History; Smithsonian National Museum of Natural History; Museu de Zoologia da Universidade de São Paulo; Universidade

DRAFT

Federal do Piauí. We also thank EvoClub_BR discussion group and the members of Uyeda's Lab (Virginia Tech) for thoughtful comments and suggestions to the text. This work was partially supported by grants from NSF to FAM (DEB 1350474 and DEB 1942717) and FAPESP to AH and GM (2012/24937-9; 2011/14295-7).

1. Lande R (1979) Quantitative genetic analysis of multivariate evolution, applied to brain: body size allometry. *Evolution* 33(1):402–416.
2. Turelli M, Gillespie JH, Lande R (1988) Rate tests for selection on quantitative characters during macroevolution and microevolution. *Evolution* 42(5):1085–1089.
3. Hansen T, Houle D (2008) Measuring and comparing evolvability and constraint in multivariate characters. *Journal of Evolutionary Biology* 21(5):1201–1219.
4. Leinonen T, McCairns RJS, O'Hara RB, Merilä J (2013) QST–FST comparisons: evolutionary and ecological insights from genomic heterogeneity. *Nature Publishing Group* pp. 1–12.
5. Lynch M (1990) The rate of morphological evolution in mammals from the standpoint of the neutral expectation. *The American Naturalist*.
6. Lande R (1986) The dynamics of peak shifts and the pattern of morphological evolution. *Paleobiology*.
7. Lemos B, Marroig G, Cerqueira R (2001) Evolutionary rates and stabilizing selection in large-bodied opossum skulls (Didelphimorphia: Didelphidae). *Journal of Zoology* 255(2):181–189.
8. Hansen TF, Solvin TM, Pavlicev M (2019) Predicting evolutionary potential: A numerical test of evolvability measures. *Evolution* 276:1182–15.
9. Schroeder L, von Cramon-Taubadel N (2017) The evolution of hominoid cranial diversity: A quantitative genetic approach. *Evolution* 71(11):2634–2649.
10. Grabowski M, Roseman CC (2015) Complex and changing patterns of natural selection explain the evolution of the human hip. *Journal of Human Evolution* 85(C):94–110.
11. Butler MA, King A (2004) Phylogenetic comparative analysis: a modeling approach for adaptive evolution. *The American Naturalist* 164(6):683–695.
12. Revell LJ, Mahler DL, Peres-Neto PR, Redelings BD (2011) A new phylogenetic method for identifying exceptional phenotypic diversification. *Evolution* 66(1):135–146.
13. Delsuc F, et al. (2016) The phylogenetic affinities of the extinct glyptodonts. *Current Biology* 26(4):R155–R156.
14. Ackermann RR, Cheverud JM (2002) Discerning evolutionary processes in patterns of tamarin (genus *Saguinus*) craniofacial variation. *American Journal of Physical Anthropology* 117(3):260–271.
15. Marroig G, Cheverud JM (2004) Did natural selection or genetic drift produce the cranial diversification of neotropical monkeys? *The American Naturalist* 163(3):417–428.
16. Hallgrímsson B, et al. (2009) Deciphering the palimpsest: studying the relationship between morphological integration and phenotypic covariation. *Evolutionary Biology* 36(4):355–376.
17. Shirai LT, Marroig G (2010) Skull modularity in neotropical marsupials and monkeys: size variation and evolutionary constraint and flexibility. *Journal of Experimental Zoology Part B: Molecular and Developmental Evolution* 314B(8):663–683.
18. Marroig G, Cheverud JM (2010) Size As A Line Of Least Resistance II: Direct Selection On Size Or Correlated Response Due To Constraints? *Evolution* 64(5):1470–1488.
19. Goswami A, Smaers JB, Soligo C, Polly PD (2014) The macroevolutionary consequences of phenotypic integration: from development to deep time. *Philosophical Transactions of the Royal Society B: Biological Sciences* 369(1649):20130254.
20. Owen R (1838) Fossil mammalia in *The Zoology of the voyage of H.M.S. Beagle, under the command of Captain Fitzroy during the years 1832–1836.*, ed. Darwin C. (Smith Elder and Co, London), p. 111 pp.
21. Fariña RA, Vizcaíno S (2001) Carved teeth and strange jaws: how glyptodonts masticated. *Acta Palaeontologica Polonica* 46(2):219–234.
22. Vizcaíno SF, Cassini GH, Fernicola JC, Bargo MS (2011) Evaluating Habitats and Feeding Habits Through Ecomorphological Features in Glyptodonts (Mammalia, Xenarthra). *Ameghiniana* 48(3):305–319.
23. Simpson GG (1944) *Tempo and mode in evolution.* (Columbia University Press: New York) No. 15.
24. Polly PD (2008) Adaptive Zones and the Pinniped Ankle: A Three-Dimensional Quantitative Analysis of Carnivoran Tarsal Evolution. pp. 167–196.
25. Hoffstetter R (1958) *Xenarthra. Traité de paléontologie mammifères évolution.* (Paris, France: Masson et Cie).
26. Fernicola JC, Porpino KO (2012) Exoskeleton and Systematics: A Historical Problem in the Classification of Glyptodonts. *Journal of Mammalian Evolution* 19(3):171–183.
27. Mitchell KJ, et al. (2016) Ancient DNA from the extinct South American giant glyptodont Doedicurussp. (Xenarthra: Glyptodontidae) reveals that glyptodonts evolved from Eocene armadillos. *Molecular Ecology* 25(14):3499–3508.
28. Hubbe A, Melo D, Marroig G (2016) A case study of extant and extinct Xenarthra cranium covariance structure: implications and applications to paleontology. *Paleobiology* 42(3):465–488.
29. Jolicoeur P (1963) The Multivariate Generalization of the Allometry Equation. *Biometrics* 19(3):497–499.
30. Felsenstein J (1985) Phylogenies and the comparative method. *The American Naturalist* 125(1):1–15.
31. Machado FA, Hubbe A, Melo D, Porto A, Marroig G (2019) Measuring the magnitude of morphological integration: The effect of differences in morphometric representations and the inclusion of size. *Evolution* 33:402–11.
32. Slater GJ, Friscia AR (2019) Hierarchy in adaptive radiation: A case study using the Carnivora (Mammalia). *Evolution* 73(3):524–539.
33. Segura V, Cassini GH, Prevosti FJ (2021) Evolution of Cranial Ontogeny in South American Canids (Carnivora: Canidae). *Evolutionary Biology* pp. 1–20.
34. Hohenlohe PA, Arnold SJ (2008) MIPoD: A Hypothesis-Testing Framework for Microevolutionary Inference from Patterns of Divergence. *The American Naturalist* 171(3):366–385.
35. Machado FA (2020) Selection and constraints in the ecomorphological adaptive evolution of the skull of living Canidae (Carnivora, Mammalia). *The American Naturalist* -(-):1–20.
36. Rossoni DM, Assis APA, Giannini NP, Marroig G (2017) Intense natural selection preceded the invasion of new adaptive zones during the radiation of New World leaf-nosed bats. *Scientific Reports* 7(1):1–11.
37. Cardini A, Polly PD (2013) Larger mammals have longer faces because of size-related constraints on skull form. *Nature Communications* 4:2458.
38. Vizcaíno SF, Fariña RA, Fernicola JC (2009) Young Darwin and the ecology and extinction of Pleistocene South American fossil mammals. *Revista de la Asociación Geológica Argentina* 66(1):160–169.
39. Melchionna M, et al. (year?) Macroevolutionary trends of brain mass in Primates. *Biological Journal of the Linnean Society* p. 2020.
40. Witmer LM (1995) The extant phylogenetic bracket and the importance of reconstructing soft tissues in fossils in *Functional morphology in vertebrate paleontology*, ed. Thomason J. pp. 19–33.
41. Felsenstein J (1988) Phylogenies and quantitative characters. *Annual Review of Ecology and Systematics* 19:445–471.
42. De Magalhaes J, Costa J (2009) A database of vertebrate longevity records and their relation to other life-history traits. *Journal of evolutionary biology* 22(8):1770–1774.
43. Vizcaíno SF, Blanco RE, BENDER JB, Milne N (2010) Proportions and function of the limbs of glyptodonts. *Lethaia* 44(1):93–101.
44. Lorenzen ED, et al. (2011) Species-specific responses of Late Quaternary megafauna to climate and humans. *Nature* 479(7373):359–364.
45. Schluter D, Price T, Mooers AØ, Ludwig D (1997) Likelihood of ancestor states in adaptive radiation. *Evolution* pp. 1699–1711.
46. Cheverud JM (1988) A comparison of genetic and phenotypic correlations. *Evolution* 42(5):958–968.
47. Garcia GRG, Hingst-Zaher E, Cerqueira R, Marroig G (2014) Quantitative Genetics and Modularity in Cranial and Mandibular Morphology of Calomys expulsus. *Evolutionary Biology* 41(4):619–636.
48. Porto A, et al. (2015) Rate of evolutionary change in cranial morphology of the marsupial genus *Monodelphisis* constrained by the availability of additive genetic variation. *Journal of Evolutionary Biology* 28(4):973–985.
49. Turelli M (1988) Phenotypic evolution, constant covariances, and the maintenance of additive variance. *Evolution* 42(6):1342–1347.
50. Marroig G, Melo DAR, Garcia GRG (2012) Modularity, noise, and natural selection. *Evolution* 66(5):1506–1524.

DRAFT

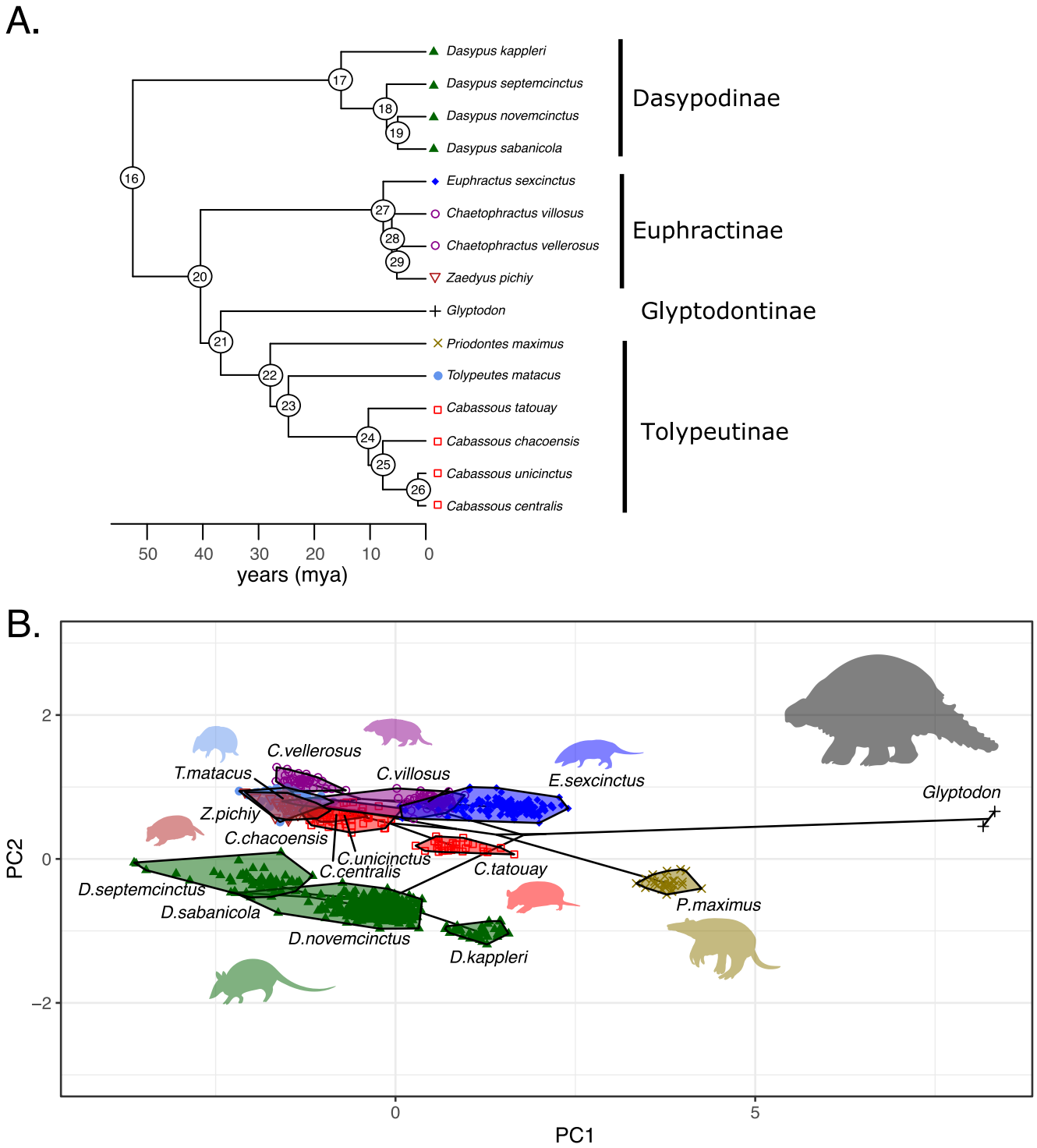

Fig. 1. **A.** Cingulata phylogeny, including the extinct *Glyptodon* (13). Numbers represents the node names refered throughout our analyses. **B.** Principal component analysis (PCA) of the 33 morphometric measurements of the skull of Cingulata species. Convex polygons encapsulates each individual species. Symbols and colors identify genus as shown in **A**. Silhouettes kindly produced by M. C. Luna.

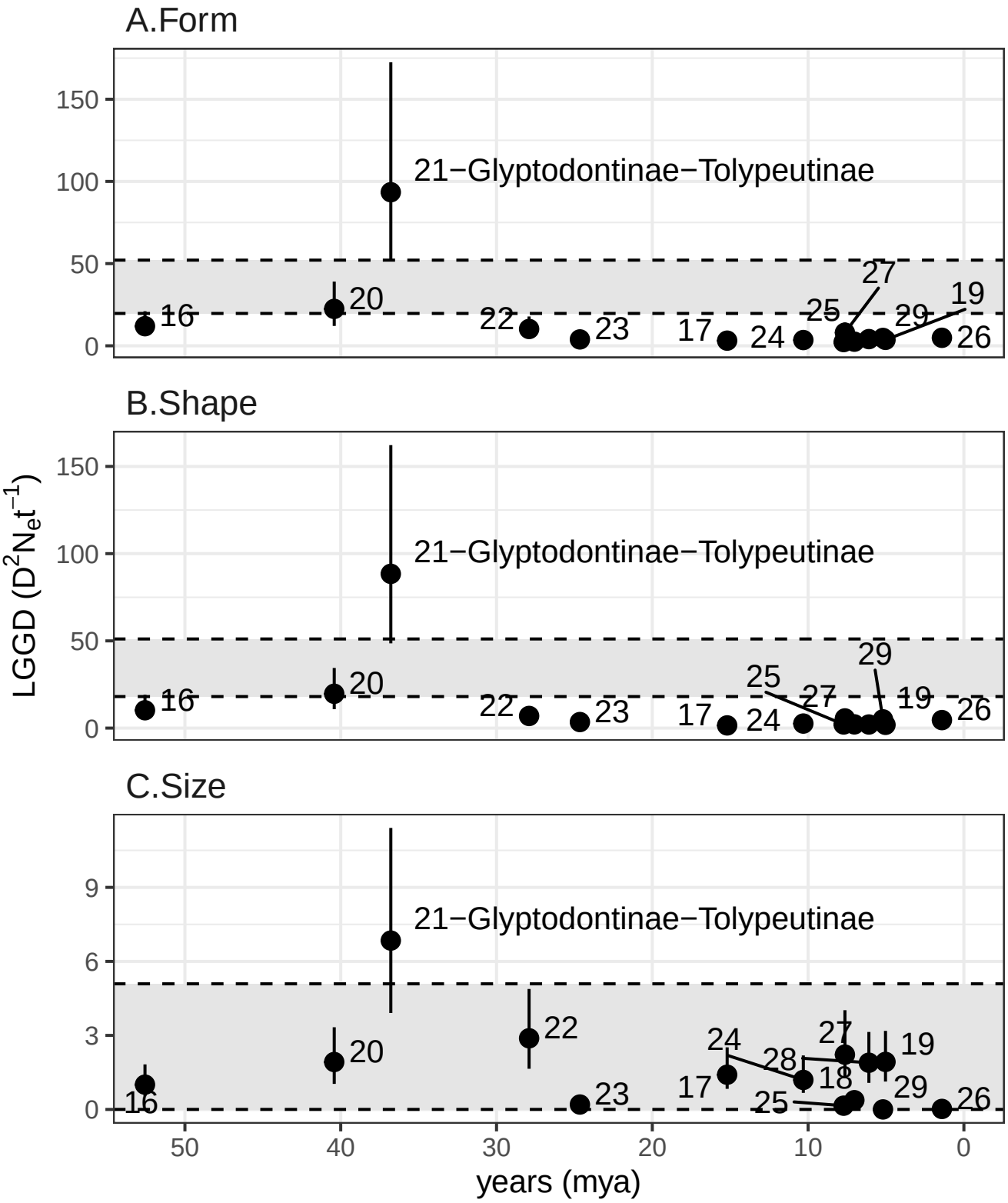

Fig. 2. Values for Lande's Generalized Genetic Distance (LGGD) calculated at each node plotted against node age for form (**A.**), shape (**B.**) and size (**C.**). Dots and solid lines represent the median and the ranges for the LGGD values for a given node. Nodes are numbered following Figure 1A. Gray area represents the expectation under drift. Values above it are consistent with directional selection and below it with stabilizing selection.

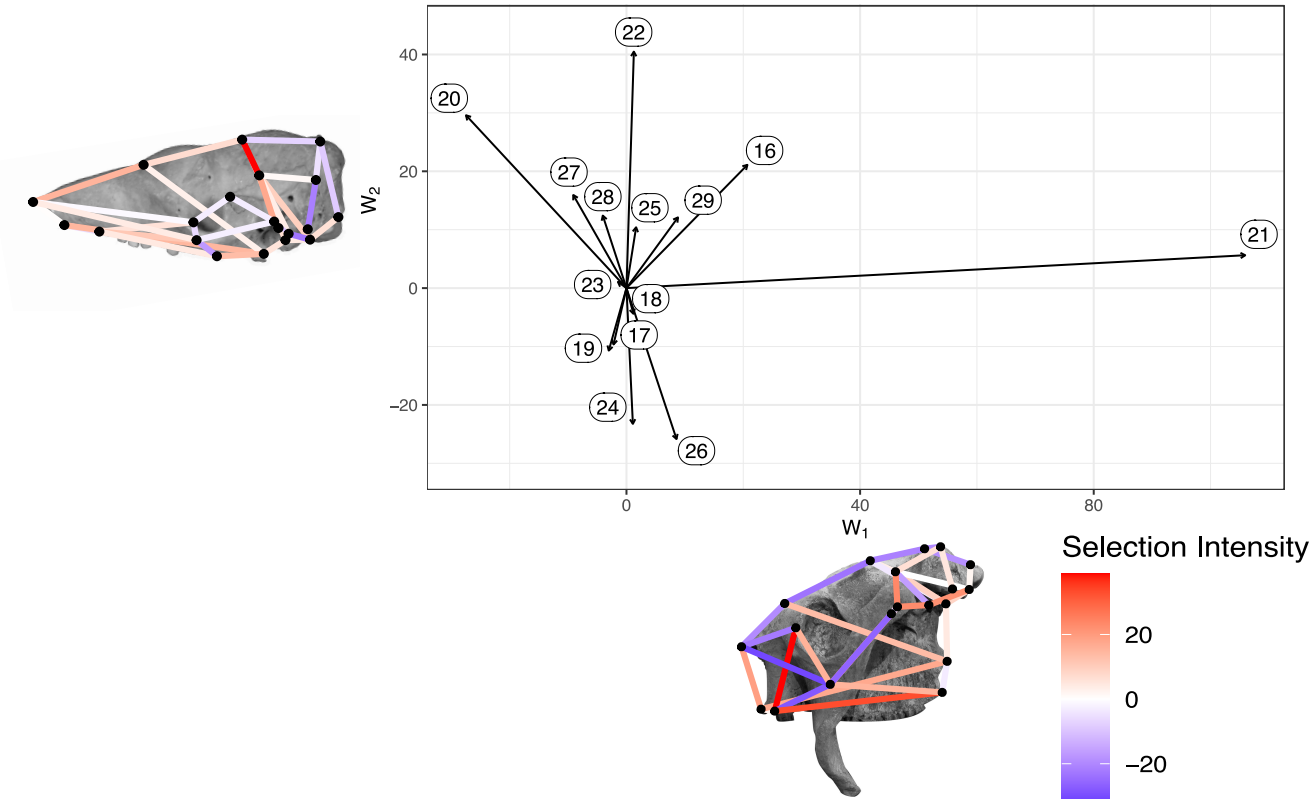

Fig. 3. Projection of node-wise selection gradients on the two main predominant directions of directional selection (W_1 and W_2). Numbers represent the nodes on the phylogeny (Fig. 1A). Skulls depict a graphical representation of the two main directions W_1 (*Glyptodon* skull) and W_2 (*Cabassous* skull). Colors represents the intensity and direction (blue-negative and red-positive) of selection.

Supplementary methods and Results

Sample and measurements. We obtained morphometric variables from skulls belonging to 14 extant and one extinct species, representating of four Cingulata subfamilies (Table S1). Only adult individuals were sampled. Criteria used to determine adulthood are explained in (28).

Table S1. Sample size by species.

Subfamily	Species	sample
Dasypodinae	*Dasypus kappleri*	34
	Dasypus novemcinctus	341
	Dasypus sabanicola	2
	Dasypus septemcinctus	52
Tolypeutinae	*Cabassous centralis*	9
	Cabassous chacoensis	2
	Cabassous tatouay	30
	Cabassous unicinctus	37
	Tolypeutes matacus	39
	Priodontes maximus	30
Glyptodontinae	*Glyptodon*	2
Euphractinae	*Chaetophractus vellerosus*	47
	Chaetophractus villosus	65
	Euphractus sexcinctus	125
	Zaedyus pichiy	45
	TOTAL	860

Landmarks are the same as in (28, Fig S1). The set o measurements refer to the 35-measurements found in (28) minus two measurements: PT-TSP and APET-TS. These measurements were excluded because they can sometimes reach small values on some species, and their variance is disproportionately inflated on the log scale. See (28) for more information on landmark and measurement description, data processing, and measurement repeatabilities.

Phylogeny. The phylogenetic relationships between species were based on molecular analysis on mitogenomic data from Delsuc et al. (13; fig 1C), consistent with other independently derived analysis (27). Both papers determined the placement of Gliptodonts on the Xenarthran phylogeny based on ancient DNA samples extracted from *Doedicurus* sp specimens. Here, we swapped *Doedicurus* sp. for *Gliptodon* sp. because there is ample evidence showing that both belong to the same subfamily (20, 25). In the absence of any other member of the group in our analysis, the phylogenetic position of one glyptodontid can be assigned to any other species of that clade. Furthermore, because both species are thought to have gone extinct at roughly the same time (around the end of the Pleistocene and the beginning of the Holocene), there is no need to scale branch lengths accordingly.

Generation time. Generation times were obtained (42) by summing up the timing of sexual maturity of females and the incubation period. Because armadillos reproduce more than once throughout their lifetimes, real generation times are probably larger than this. As a consequence of our calculations, the values used here for generation times are considered a minimum benchmark value and not the true one. Furthermore, because larger generation times imply that fewer generations have transpired during the same period, this means that our estimates of LGGD are probably underestimated. Given that small LGGD are consistent with stabilizing selection and that stabilizing selection is expected to be the dominant force in the evolution of morphological traits, the use of these underestimated generation times leads to conservative estimates of LGGDs.

Type I error rates for LGGD. To access the adequacy of the parametric test proposed for the Lande's Generalized Genetic Distance (1), we employed a simulation approach. We generated 10,000 rounds of one generation neutral multivariate evolution using equation 2 and known parameters for $\bar{h^2}$ and N_e. For each simulated vector of divergence, we resampled $\mathbf{P}$ using a Monte-Carlo approach to simulate sampling error. $\mathbf{P}$s were reestimated with the same original empirical sample (n=860). Because the calculation of LGGDs involves the inversion of

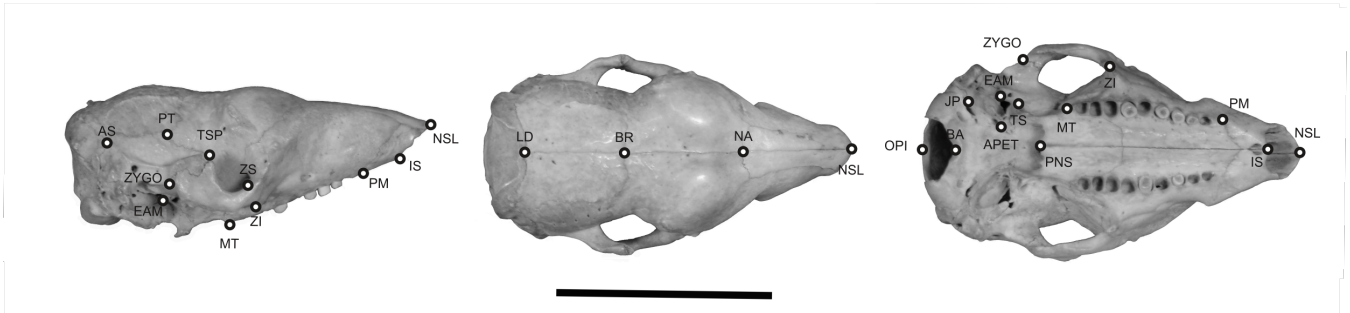

Fig. S1. Cranial landmarks measured in this study represented on a *Cabassous* specimen. Bar is equal to 5 cm.

DRAFT

Table S2. Loadings of the first two principal components of the intra and interespecific morphometric datasets. Traits are discriminated according to their cranial anatomical regions.

		Intraspecific		Interespecific	
Trait	Anatomical region	PC1	PC2	PC1	PC2
IS.PM	Face	0.194	0.058	0.178	-0.017
IS.NSL	Face	0.200	0.012	0.200	-0.031
IS.PNS	Face	0.175	0.033	0.175	-0.209
PM.ZS	Face	0.169	0.159	0.153	-0.337
PM.ZI	Face	0.165	-0.041	0.139	-0.315
PM.MT	Face	0.162	0.054	0.172	-0.114
NSL.NA	Face	0.183	0.101	0.178	-0.197
NSL.ZS	Face	0.177	0.132	0.160	-0.225
NSL.ZI	Face	0.175	-0.016	0.153	-0.217
NA.PNS	Face	0.170	0.002	0.175	-0.123
PT.ZYGO	Face	0.219	0.000	0.195	-0.118
ZS.ZI	Face	0.213	-0.904	0.126	-0.029
ZI.MT	Face	0.212	-0.009	0.189	0.275
ZI.ZYGO	Face	0.197	0.291	0.239	0.298
ZI.TSP	Face	0.244	0.138	0.235	0.207
MT.PNS	Face	0.181	-0.055	0.190	-0.340
EAM.ZYGO	Face	0.181	-0.027	0.195	0.095
ZYGO.TSP	Face	0.236	0.004	0.213	0.166
NA.BR	Neurocranium	0.171	0.021	0.161	-0.162
BR.PT	Neurocranium	0.090	-0.009	0.126	-0.021
BR.APET	Neurocranium	0.141	0.012	0.142	0.019
PT.APET	Neurocranium	0.136	0.015	0.141	0.041
PT.BA	Neurocranium	0.140	0.005	0.157	0.048
PT.EAM	Neurocranium	0.160	-0.003	0.181	0.076
PNS.APET	Neurocranium	0.204	0.075	0.189	0.015
APET.BA	Neurocranium	0.139	0.009	0.174	0.131
BA.EAM	Neurocranium	0.140	0.027	0.180	0.287
LD.AS	Neurocranium	0.139	-0.013	0.192	0.174
BR.LD	Neurocranium	0.133	-0.033	0.151	0.106
OPI.LD	Neurocranium	0.177	0.044	0.144	-0.026
PT.AS	Neurocranium	0.160	-0.024	0.200	0.141
JP.AS	Neurocranium	0.161	0.037	0.146	0.043
BA.OPI	Neurocranium	0.076	-0.010	0.115	-0.059

DRAFT

the **G**, we also evaluated if a matrix extension could improve the estimation of LGGDs. The simulated and observed values of LGGD were confronted against the 95% interval under the null hypothesis following a χ-square distribution with 33 degrees of freedom (1).

Results show that in the original simulated LGGD (calculated directly from the simulated divergence and input parameters), the rejection rate of the null hypothesis using the parametric method is close to the nominal rate (rate=0.053). However, with sampling error, larger LGGDs seem to be moderately exaggerated (fig. S3A), leading to inflated type I error rates (rate of rejection of the null hypothesis=0.062). Extensions of the **G** prior to inversion led to underestimated LGGDs (fig. S3B) and to even higher type I error rates (rates=0.669). This result shows that matrix extension does not constitute a solution to sampling errors in this case (but see below). Therefore, we adapted a simulation approach to construct a non-parametric confidence interval for the null hypothesis of evolution under drift.

Matrix inversion and extension. To evaluate the potential effects of sampling error of **G** on the estimation of selection gradients (β), we performed two analyses. The first is the evaluation of the noise-floor limit, as suggested by (50). In this analysis, we evaluate the behavior of the second derivative of a discrete function defined as the relationship between the rank of an eigenvalue and the variance of eigenvalues defined by binning five neighboring eigenvalues. The noise floor limit is reached when the second derivative of this function approaches zero, and the eigenvalue rank in which this occurs is set to be the cutoff value for the extension method (50). Here we defined the noise-floor region at $1e-07$, suggesting that the first 21 eigenvalues should be maintained, and the remaining should be extended (fig. S4A).

To validate this analysis, we replicated (50) simulations, in which a known β was re-estimated on a new matrix resampled adopting a Monte Carlo approach (see 35 as well). We performed this simulation by changing the number of retained eigenvalues from 6 to 30. In each case, we performed the simulation 1000 times (25,000 simulations in total). For each simulation, we calculated the vector correlation between the original and the estimated β. Higher values imply that the estimated β is in the same direction as the original simulated selection gradient. From 6 to 21 eigenvectors, the correlation between original and estimated selection gradients increased almost steadily, reaching a plateau from 21 to 26 eigenvalues (Figure S4B). After 26 vectors, the vector correlation starts to decrease, suggesting that

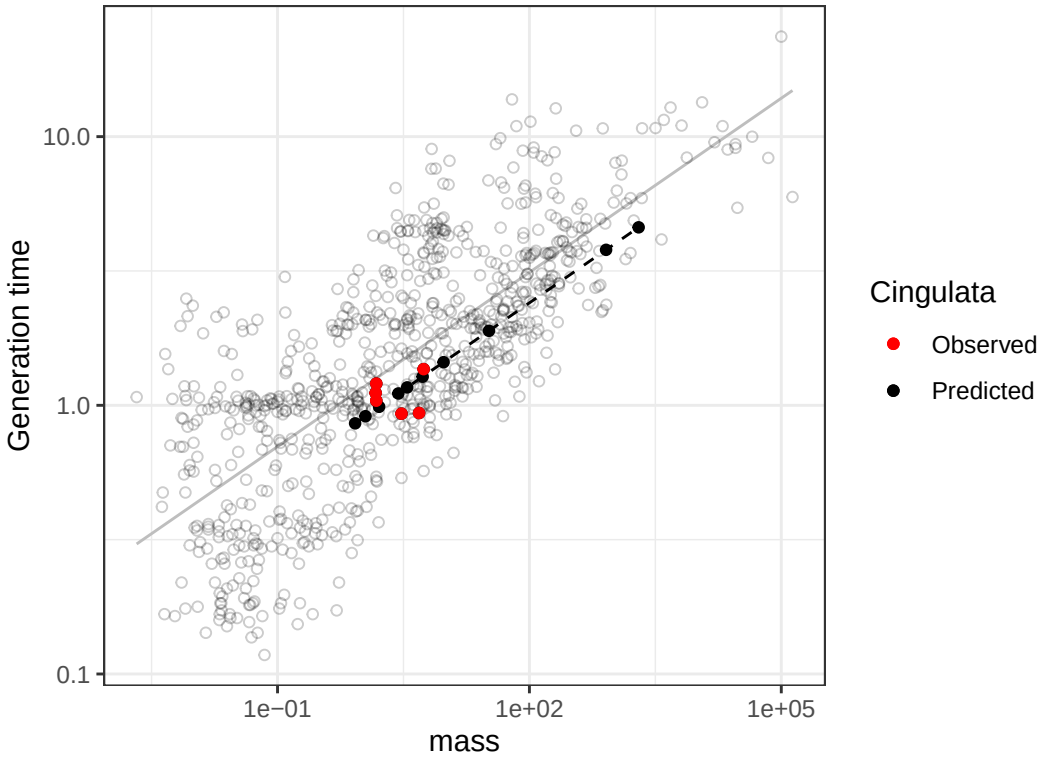

Fig. S2. Relationship between generation time and body mass for 805 mammalian species. Solid gray line represents the linear relationship for all species. Red filled circles represent Cingulata taxa with both mass and generation time information. Black filled circles represent Cingulata taxa with only mass, and with a predicted generation time. Dashed line represents the model adopted for the association between mass and generation time among Cingulata.

DRAFT

retaining more vectors leads to badly estimated βs. We chose to keep 21 vectors because it is the first eigenvalue to reach the noise-floor on the previous analysis. Furthermore, estimations of the selection gradient to generate a glyptodont morphology did not significantly change with the retention of more axes.

Adaptive landscape and selective lines of least resistance. In a quantitative genetics framework, adaptive landscapes can be investigated as the variance-covariance matrix of adaptive peaks (18, 34, 35, 41). Following (35), we calculated this matrix as follows

$$\Omega = \mathbf{G}^{-1}\Delta z \Delta z^t \mathbf{G}^{-1}\frac{1}{n} \qquad [S1]$$

With n being the species sample size. This equation is equal to the cross-products of the selection gradients. The *ith* eigenvectors of Ω (W_i) can be interpreted as predominant directions of directional selection and the projection of node-specific βs can be interpreted as the loading of a specific gradient to that axis.

Following (35), we performed a Monte-Carlo simulation approach to investigate which axes could be considered different from neutral evolution. This was done using equation 2 to generate 10,000 datasets under drift. For each round of the simulation, Ω was calculated and its eigenvalues were obtained. The resulting Ω was scaled to have the same trace as the empirical one, so we only consider the distribution of eigenvalues, not their absolute magnitude. The distribution of eigenvalues of the simulations was then confronted to the empirical eigenvalues and those that were greater than 95% than the simulated ones were considered significant.

Because the Glyptodont divergence dominates the dataset, we performed two different sets of simulations. One where we included Glyptodont to calculate the empirical trace of Ω, and one where it was excluded. For the simulations including Glyptodont, only the first leading eigenvalue was considered significant, while the exclusion of glyptodonts showed that the three leading axes are significant (Fig. S5). An investigation of the scores of node-specific βs on W_3 shows that the only nodes with high scores are nodes 28 and 29 (Fig. S6A). These nodes represent the divergences among *Chaetophractus* and *Zaedyus* species. The multivariate representation of the selection gradients shows mainly a concentrated pressure to expand the nasal cavity and increase the distance between the anterior-most portion of the zygomatic arch and the tip of the snout (Fig. S6B). This representation matches the described differences of *Zaedyus* in relation to *Chaetophractus*. Because this axis is so phylogenetically restricted, we focus on the leading two directions on the main text.

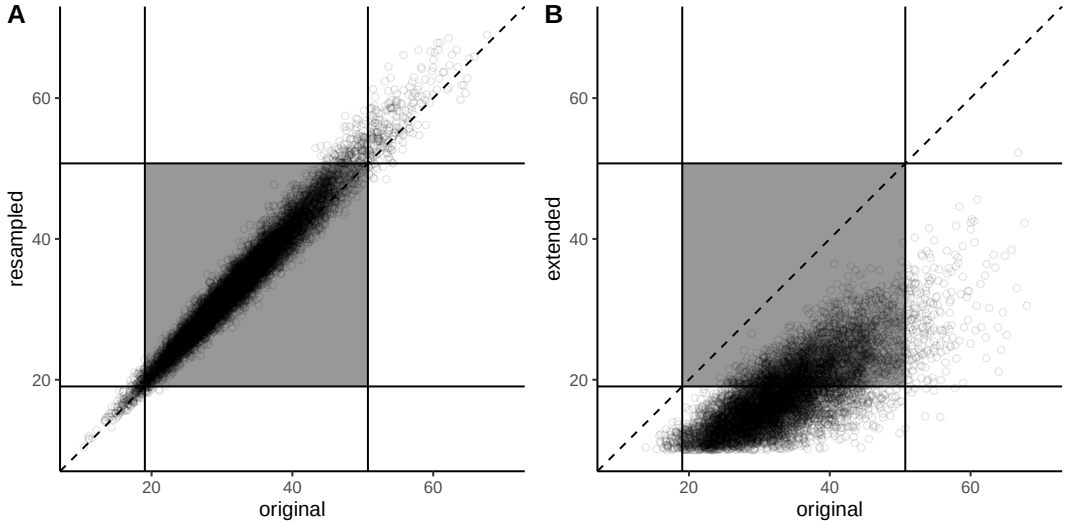

Fig. S3. Relationship between actual (original) and estimated LGGD for resampled matrices without (**A**) and with extension (**B**), respectively. The dark quadrant represents the 95% theoretical intervals for the null-hypothesis under drift for both the original and resampled matrices. The dashed line represents the line in which observed and original values are equal.

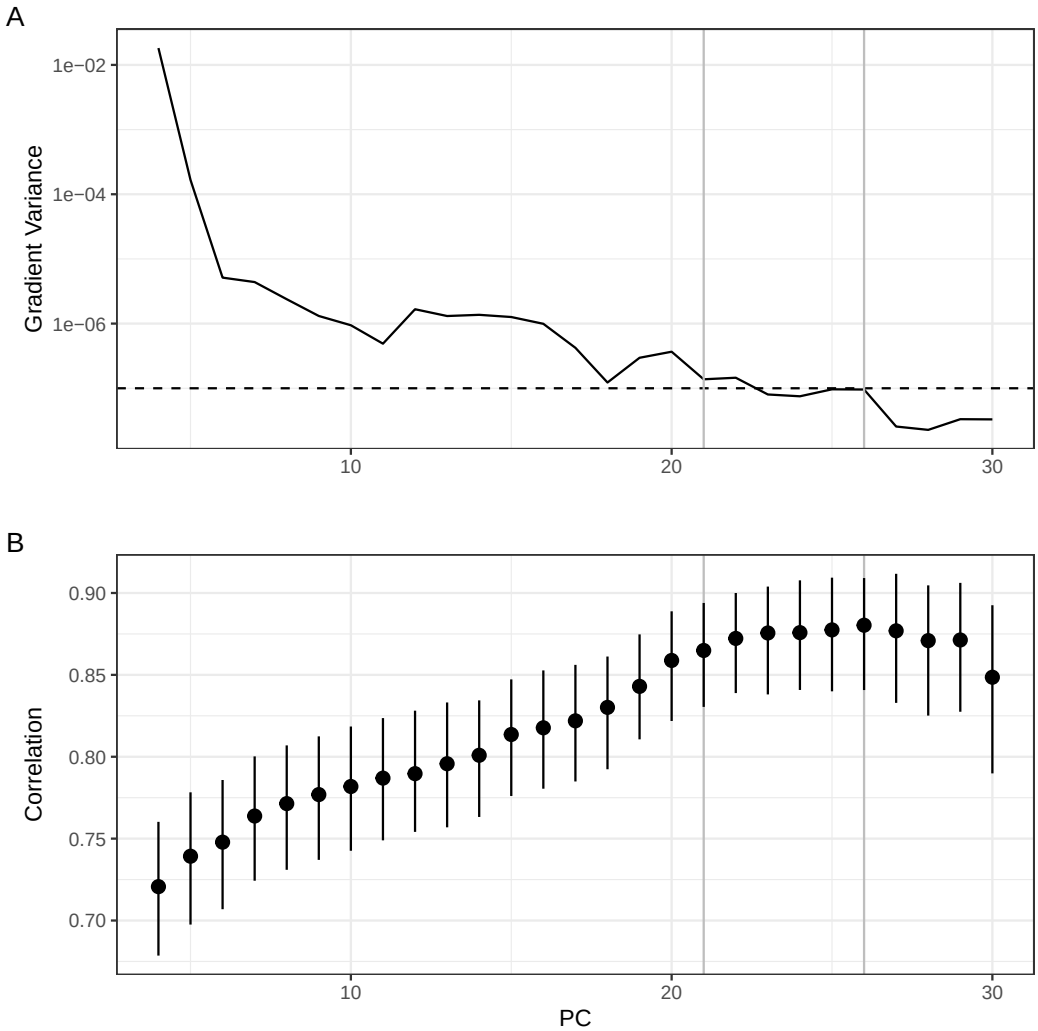

Fig. S4. A. Noise floor analysis for the pooled within-group covariance matrix for Cingulata. **B**. Correlation between original and estimated βs on the simulation approach. Horizontal grey lines represent numbers of eigenvalues retained that show high vector correlation between original and estimated βs and are near the noise floor.

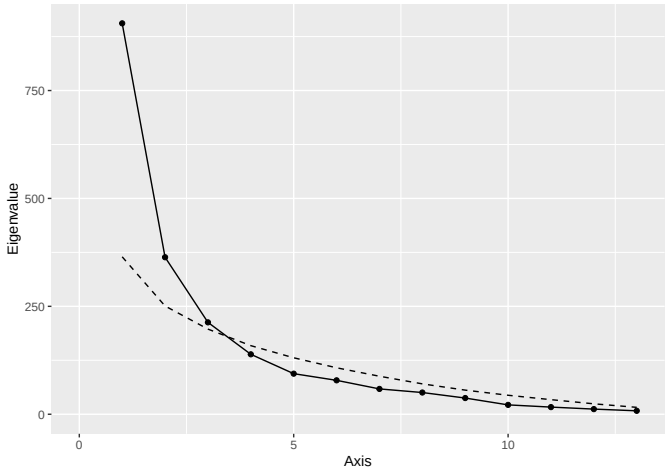

Fig. S5. Empirical (solid line) and simulated (dotted line) distribution of Ω's eigenvalues.

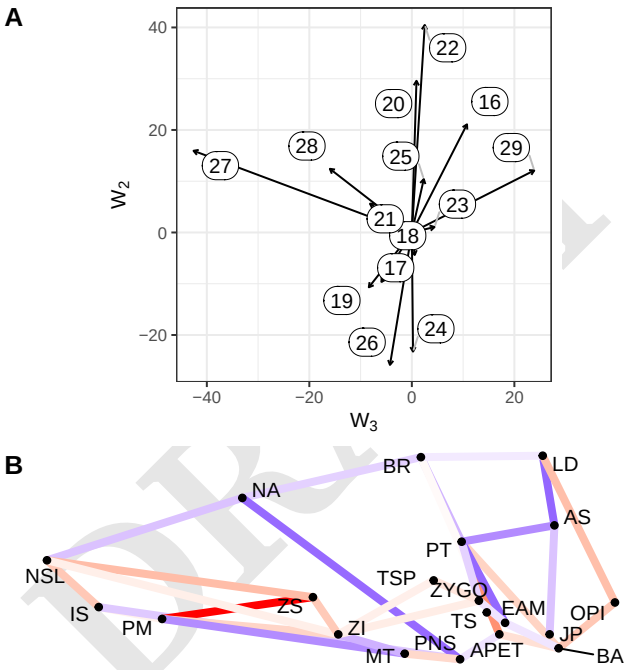

Fig. S6. A. Projection of node-wise selection gradients on the two main predominant directions of directional selection (W_3 and W_2). Numbers represent the nodes on the phylogeny (Fig. 1A). **B**. Graphical representation of W_3. Color represents the intensity of positive (red) and negative (blue) selection, as in Fig. 3.